



Selective formation of reactive oxygen species in peroxymonosulfate activation by metal-organic framework-derived membranes: A defect engineering-dependent study

Mohua Li ^a, Shijie You ^{b,*}, Xiaoguang Duan ^c, Yanbiao Liu ^{a,*}

^a College of Environmental Science and Engineering, Textile Pollution Controlling Engineering Center of the Ministry of Ecology and Environment, Donghua University, Shanghai 201620, China

^b State Key Laboratory of Urban Water Resource and Environment, School of Environment, Harbin Institute of Technology, Harbin 150090, China

^c School of Chemical Engineering and Advanced Materials, The University of Adelaide, Adelaide 5005, SA, Australia



ARTICLE INFO

Keywords:

Oxygen vacancy
Defect engineering
Peroxymonosulfate activation
Singlet oxygen
Surface chemistry

ABSTRACT

Defect engineering is an effective way to unveil relationship within structures and catalytic activities of transition metal oxides. Herein, a novel strategy has been developed for *in situ* generation and controlling oxygen vacancy (Ov) levels in a host lattice by varying oxygen pressure during calcination of zeolitic imidazolate framework-67 (ZIF-67) membranes. The as-prepared NFZ-5 membrane with the largest Ov content (δ , 0.912) gave the highest $^1\text{O}_2$ production (98.3%) and PMS activated BPA degradation kinetics ($k = 0.11 \text{ min}^{-1}$). Advanced characterization and density functional theory (DFT) calculations have revealed the pivotal role of Ov in modifying surface chemistry of the catalytic membrane *via* enhancing the number of *Lewis* acid sites. These *Lewis* acid sites have facilitated the chemisorption of peroxymonosulfate (PMS) onto membrane, and the resulting reactive intermediate complexes have altered the electron transfer direction between PMS and the catalyst.

1. Introduction

Emerging micropollutants are anthropogenic chemicals that originate from a wide range of sources to accumulate in low concentrations (ng/L to $\mu\text{g}/\text{L}$) in aquatic environments [1,2]. Hence, micropollutants have raised global concerns because of their potential deleterious effects on environment and human health. The removal of trace levels of micropollutants from wastewater by using conventional treatment technology is challenging because of limitations associated with mass transport and degradation kinetics [3]. Advanced oxidation processes (AOPs) based on PMS activation offer a strategy to degrade micropollutants *via* nonradical/ radical pathways [4–6]. Although PMS can be activated by using light, heat, ultrasound, electricity, transition metals and other catalysts, these approaches are limited because of high energy involvement and formation of huge secondary pollutants [7]. Therefore, the development of cost-effective and low environmental impact strategies for PMS activation has become dominantly crucial.

Oxygen vacancies (Ov) are the most common defects found in semiconducting metal oxides [8]. Previous studies have shown the essential role of Ov in various catalytic systems, such as photocatalysis [9,10],

electrocatalysis [11,12], and piezoelectric catalysis [13,14]. In principle, the presence of abundant localized electrons associated with Ov facilitates the sorption of O_2 , thereby generating reactive oxygen species (ROSs) [15]. This mechanism may also be applied for PMS activation because of its similar O–O bond structure. Bu et al. reported that Ov on BiOBr powders fluently activated peroxydisulfate *via* nonradical pathway ($^1\text{O}_2$) [16], whereas radical pathway ($\text{SO}_4^{\cdot-}$) appeared to dominate PMS activation using Ov-enriched Co-doped TiO_2 nanotubes [17,18]. Such paradox has illustrated the necessity for specific approaches to quantitatively fine-tune Ov concentration of metal oxides for smooth PMS activation. In addition, the practical application of these reported powder-like catalysts was restricted by agglomeration and requirement for post-utilization separation.

Therefore, metal-organic frameworks (MOFs) have been selected herein as ideal platform to design a series of Co_3O_4 -based catalytic membranes with defined Ov concentrations. The catalytic membranes have then been used to demonstrate the regulation of PMS activation from radical pathway in the Ov-deficient state to a nonradical pathway in the Ov-enriched state. To achieve this target, a facile electrochemical strategy was initially employed for the *in-situ* growth of ZIF-67 on a Ni

* Corresponding authors.

E-mail addresses: sjyou@hit.edu.cn (S. You), yanbiaoliu@dhu.edu.cn (Y. Liu).

foam, since Ni shared similar physicochemical properties to Co (the centrally-coordinated metal ion of ZIF-67). ZIF-67 ($C_8H_{10}N_4Co$) does not contain oxygen and Co is present in various oxidation states, Ov can be generated spontaneously because 2-methylimidazole (2-MeIM) ligands extract neighboring O atoms, especially at the lower O_2 conditions. Hence, ZIF-67 serves as a self-sacrificed template for synthesizing Ov-enriched Co_3O_4 in oxidative atmosphere, in which δ values can be tuned by manipulating the partial pressure of oxygen during heat treatment. Herein, BPA has been chosen as a model micropollutant to determine the potential of the Ov-mediated PMS activation system operating in a flow-through configuration. The mechanism for PMS activation and BPA degradation has been elucidated in detail based on experimental results and DFT calculations. To the best of our knowledge, the optimization of δ values via controlled oxygen pressure strategy has not been reported yet. This study provides a novel strategy for the development of Ov-mediated PMS activation systems with selective generation of ROS for micropollutants remediation. It also gives new insights into the surface chemistry-activity relationships and demonstrates the practical efficiency of a continuous-flow configuration for removing micropollutants.

2. Experimental section

2.1. Chemicals

Ni-foam (> 98%; thickness = 0.5 mm) was obtained from Lizhiyuan Electronics Co., Ltd. (Shanxi, China). All chemicals were of AR grade and used without further purification. Cobalt nitrate hexahydrate ($Co(NO_3)_2 \cdot 6 H_2O$, 99.9%), 2-MeIM ($C_4H_6N_2$), BPA, methanol (MeOH, 99.9%), acetone (99.8%), hydrochloric acid (HCl, 36–38%), nitric acid (68%), 1,3-diphenylisobenzofuran (97%), benzoic acid (BA, 99%), *p*-hydroxybenzoic acid (99%), *p*-benzoquinone (99%), methyl phenyl sulfoxide (PMSO), methyl phenyl sulfone (PMSO₂), potassium iodide (KI), 2,2,6,6-tetramethyl-4-piperidinol (TEMP, 96%), 5,5-dimethyl-1-pyrroline-n-oxide (DMPO, 97%), furfuryl alcohol (FFA, 98%), humic acid (HA, 98%), PMS, sodium phosphate dibasic dodecahydrate ($Na_2HPO_4 \cdot 12 H_2O$, 96%), sodium chloride (96%), sodium hydroxide (NaOH, 96%), sodium bicarbonate (Na_2CO_3 , 99.8%), sodium sulfate (96%), cobaltosic oxide (Co_3O_4 , 99.8%) and sodium nitrate (99%) were purchased from Sinopharm Chemical Reagent Co., Ltd. (Shanghai, China). NafionTM solution (5 wt%) was purchased from Aldrich. Lake water and pharmaceutical wastewater were collected from Jingyue lake of Donghua University and a local hospital of Shanghai, China, respectively). The characteristics of the water samples are given in Table S1. All aqueous solutions were prepared with deionized water (18.2 MΩ·cm) from a Milli-Q® Direct 8 Water Purification System (Merck KGaA, Darmstadt, Germany).

2.2. Preparation of Ni-foam-ZIF-67 (NFZ) membranes

N_2 was bubbled into solutions of 2-MeIM (50 mL of 4 mmol in MeOH; solution A) and $Co(NO_3)_2 \cdot 6 H_2O$ (50 mL of 0.5 mmol in MeOH; solution B) for 30 min to eliminate dissolved O_2 . NFZ membranes were prepared via electrochemistry-driven *in-situ* growth method by using a three-electrode system (*i.e.*, a Ni-foam working electrode of 7.1 cm²; a Pt counter electrode, and an Ag/AgCl reference electrode). The Ni foam was cleaned with acetone and methanol before immersing into solution B. Two opposing potentials were then sequentially applied, such as 1 V (vs Ag/AgCl) potential was set for 1 min, which became – 1.5 V (vs Ag/AgCl) for 20 min after the addition of solution B. The resultant NFZ membranes were washed thoroughly with methanol to remove excess ligands and salts.

2.3. Thermal preparation of NFZ-derived catalytic membranes

The as-obtained NFZ membranes were transferred into quartz boats

and sealed in a quartz tube, where oxygen could be introduced. The apparatus was placed in a tube furnace at the initial pressure of 0.1 Pa, controlled by a vacuum pump. The temperature was then increased to 450 °C at 5 °C min^{–1} and O_2 was introduced into the quartz tube at 5, 10 and 20 Pa for 2 h to obtain a series of membrane materials (designated as NFZ-5, NFZ-10, and NFZ-20, respectively). Control samples were prepared by the similar method, except that the calcination atmosphere was changed to air and N_2 (designated as NFZ-Air and NFZ-N₂, respectively). Studies related to the Co-based catalyst derived from ZIF-67 for PMS activation are listed in Table S2, and discussed in the [Supplementary Material](#).

2.4. Characterization

The crystalline phases of samples were determined by X-ray diffraction (XRD) on a D/max-2550 PC diffractometer (Rigaku, Tokyo, Japan). Surface morphology and microstructure were visualized by field emission scanning electron microscopy (FE-SEM) and transmission electron microscopy (TEM) using S-4800 FESEM (Hitachi, Japan) and JEM-2100 F TEM (JEOL, Japan) respectively. Surface chemistry was analyzed by X-ray photoelectron spectroscopy (XPS) at 1 × 10^{–9} Torr by using Escalab 250Xi (Thermo Fisher Scientific, USA). Fourier transform infrared (FTIR) spectra were recorded by a Nicolet NEXUS 670 spectrometer (Thermo Electron Corporation, Madison, USA) in the attenuated total reflection (ATR) sampling mode. The leachable Co was analyzed by inductively coupled plasma mass spectrometry (ICP-MS, Agilent 7700 s, USA).

2.5. BPA degradation experiments

Degradation experiments were conducted using BPA as a model micropollutant at ambient temperature and operated in a flow-through configuration. To eliminate contribution on the BPA removal from physical adsorption, all experiments were conducted after adsorption saturation. This was achieved by passing BPA solution (100 mL of 0.044 mM) through membranes at 1.5 mL/min for 60 min. Catalytic reaction was initiated by adding PMS through an experiment, in which BPA solution (100 mL of 0.044 mM) containing PMS (1.0 mM) solution was passed through the system. The effects of solution pH (4.5–10.5), inorganic anions (*i.e.*, SO_4^{2-} , Cl^- , HPO_4^{2-} , and HCO_3^-), and organic matter (HA) on the BPA degradation kinetics were systematically investigated. Solution pH was adjusted using 1 M NaOH and HCl solutions. Effluent samples (1.0 mL) were withdrawn at predetermined time intervals and passed through a Millipore 0.22 μ m membrane filter (Merck KGaA, Darmstadt, Germany) prior to analysis. A Co_3O_4 membrane was fabricated by depositing Co_3O_4 slurry onto a Ni-foam substrate of 7.1 cm². The slurry was prepared by mixing Co_3O_4 nanoparticles, ethanol, and Nafion® suspension (5%) at the weight ratio of 1:12:7, followed by sonication for 1 h. All kinetic experiments were conducted in triplicate. The BPA degradation intermediates were identified by LC-MS, in which samples were separated using a 1200 series HPLC coupled to a 6520 accurate mass quadrupole time-of-flight mass spectrometer fitted with an electrospray ionization source (Agilent, USA).

3. Results and discussion

3.1. Development of NFZ-derived membranes with varying Ov

The schematic representations depicting the synthesis route of NFZ-derived membranes with varying Ov concentrations and details of individual stages are given in Fig. 1a-d. The ZIF-67 was grown *in-situ* on a Ni-foam surface using an electrochemical sequence of alternating applied potentials. At first, the potential was set at 1 V (vs Ag/AgCl). Compared to the control experiment employing a foam carbon working electrode (7.1 cm²), the current density using Ni-foam as working electrode was found to increase at the identical conditions, suggesting

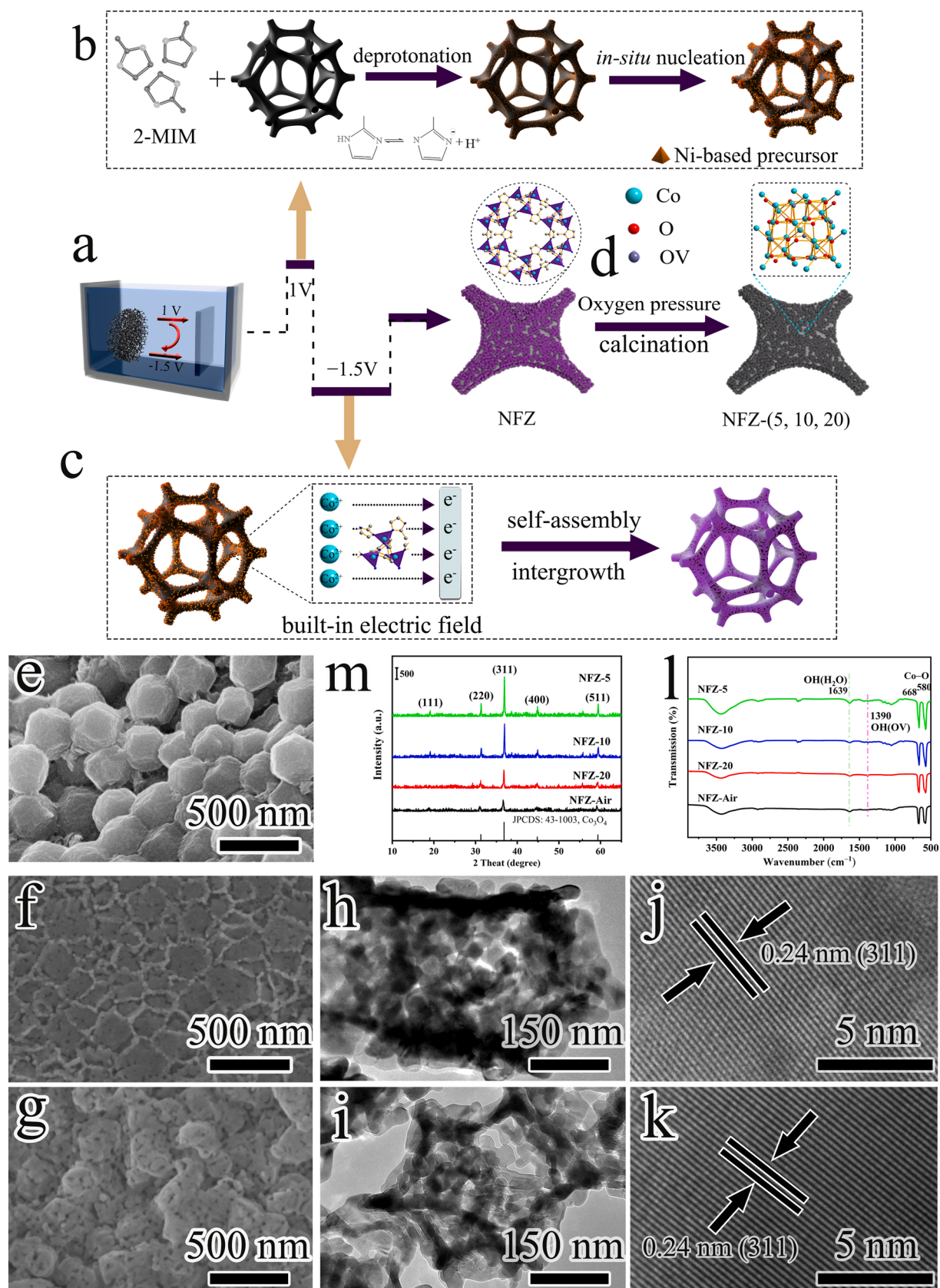


Fig. 1. Preparation and characterization of the NFZ catalytic membranes: (a) Schematic of the preparation route for the NFZ membrane; (b) *in-situ* electrochemical nucleation on Ni-foam; (c) subsequent growth of ZIF-67; (d) calcination of the NFZ membrane at different oxygen pressures (5, 10, 20 Pa); SEM images of (e) NFZ membranes, (f) NFZ-5 and (g) NFZ-Air; high-resolution TEM images of (h, j) NFZ-5 and (i, k) NFZ-Air; (m) XRD patterns and (l) ATR-FTIR spectra of the NFZ-5, NFZ-10, NFZ-20 and NFZ-Air.

oxidation of Ni. This hypothesis was supported by the elevated concentration of dissolved Ni^{2+} ($\leq 0.20 \text{ mg/L}$) measured in the effluent after 1 min of reaction. The current density of the Ni-foam electrode in a 2-MeIM/MeOH solution (red line in Fig. S1a) was twice that of the MeOH system (blue line in Fig. S1a) under anhydrous conditions in anaerobic conditions. This observation can be explained from the lower pK_a of 2-MeIM (14.4 ± 0.1) than that of methanol (15.2 ± 0.1), and the facile deprotonation of 2-MeIM. The exposed Ni substrates served as a reservoir of building blocks to coordinate with the deprotonated 2-MeIM, since the physicochemical properties of Ni and Co are identical. This resulted in the formation of a Ni-based precursor (Fig. 1b), rather than just acting as anchoring sites for ZIF-67 (e.g., reductive synthesis or electrophoretic deposition method). Fig. S1b shows that Ni-based precursor within 5–50 nm could be easily prepared from Ni substrates by the electrochemical method. After thorough washing of the as-prepared NFZ membranes with MeOH, significant alteration in color could be observed between the pristine Ni-foam (silver gray, Fig. S2a) and Ni-based precursor (yellowish-brown, Fig. S2b). The ATR-FTIR spectra of the Ni-based precursor agreed well with that of the ZIF-67 sample (Fig. S2c and Fig. S3a), indicating the successful bonding of surface exposed Ni sites with deprotonated 2-MeIM. After initial *in-situ* nucleation, the typical crystallization process of ZIF-67 formation commenced after addition of metal salts (solution B, $\text{Co}(\text{NO}_3)_2 \cdot 6 \text{ H}_2\text{O}$) and alteration of the potential to -1.5 V (vs Ag/AgCl). The introduction of anions or other probases (e.g., NO_3^- , H_2O) into the solution was necessary to increase the solution pH at the vicinity of cathode to facilitate the *in-situ* deprotonation of 2-MeIM [19]. The potential gap within metal ions (Co^{2+}) and negatively-charged deprotonated ligands could then drive the migration of Co^{2+} towards Ni-based precursor electrode because of the electrostatic attraction. The deprotonated 2-MeIM ligands could also trigger self-assembly and intergrowth of ZIF-67 crystals (Fig. 1c). Extending the growth time to 20 min led to the formation of ZIF-67 grains with the average size of $300 \pm 100 \text{ nm}$ and classic rhombic dodecahedron morphology (Fig. 1e). The XRD of NFZ membrane matched well with the simulated pattern of ZIF-67 (Fig. S3b). This indicated that the preformed Ni-based precursor posed limited effect on the crystal structure of ZIF-67. This was probably because of the similar ionic sizes of Co^{2+} (0.42 \AA) and Ni^{2+} (0.40 \AA) [20].

The ZIF-67 membranes were subsequently heated to 450°C in controlled oxygen atmosphere within 5–20 Pa (Fig. 1d). During calcination, pyrolyzation of the organic linkers (i.e., 2-MeIM) accelerated the formation of gases, such as CO_2 , CO , NO_x and/or H_2O , within ZIF-67, capable of expanding its cavity because of the internal/ external pressure differences. All calcinated products displayed the characteristic 3D mesoporous structures (Fig. 1f, g, and Fig. S4). As shown in Fig. 1f and g, ZIF-67 derivatives exhibited fair adhesion with the Ni-foam substrate. The particle size of NFZ-5 was typically within 300–400 nm while maintaining its original ZIF-67 rhombic dodecahedron framework, probably because of the slow oxidation kinetics originating from the reduced oxygen pressure (5 Pa; Fig. 1f and h). However, this observation was in contrast to the NFZ-Air, which showed evidences of rapid reaction kinetics resulting in local fracture and collapse at the high oxygen partial pressure (21278 Pa; Fig. 1g and i) in air. Despite variegated oxygen pressures experienced during calcination, Fig. 1j and k show that both NFZ-5 and NFZ-Air shared the similar spacings of Co_3O_4 (311) crystal planes (0.24 nm). The elemental mappings displayed the coexistence and distribution of Ni, Co, and O in the NFZ-5 membrane (Fig. S5). The formed Co_3O_4 nanoparticles were spread over the Ni substrate as indicated by the corresponding Co and O and Ni elemental signals.

The crystal structure and surface functional groups of NFZ-derived membranes were examined by XRD (Fig. 1m) and ATR-FTIR (Fig. 1l). The spinel structures of Co_3O_4 for the calcinated NFZ samples could be characterized by peaks at $2\theta = 19.0, 31.2, 36.8, 44.8$, and 59.3° , corresponding to {111}, {220}, {311}, {400} and {440} crystal planes, respectively (PDF: JCPDS 43–1003) [21]. The calcined product formed

from NFZ under the same annealing temperature in N_2 atmosphere was C-doped CoN (Fig. S6), which agreed with the previous report [22]. The main peaks in the ATR-FTIR spectra of these samples, calcinated under reduced oxygen atmospheres were similar to that of NFZ-Air, in which the peaks at 575 and 660 cm^{-1} were attributed to Co–O (III) and Co–O (II) moieties [23].

3.2. *Ov* characterization of NFZ-derived membranes

XPS was used to verify the association within oxygen pressure and *Ov* concentration. The characteristic O 1s peaks of all NFZ samples at 530.0, 531.5, and 532.6 eV inferred the presence of Co–O, *Ov*, and adsorbed H_2O , respectively (Fig. 2a). The relative peak area ratios of *Ov*/Co–O followed the order: NFZ-5 (0.77) > NFZ-10 (0.59) > NFZ-20 (0.47) > NFZ-Air (0.37). The Co 2p XPS of these samples contained a spin doublet ($2\text{p}_{3/2}$ and $2\text{p}_{5/2}$) of Co^{2+} at 781.3 and 797.0 eV , respectively, a doublet for Co^{3+} at 779.7 and 794.8 eV , and satellite peaks at 787.9 and 804.6 eV [21]. Generally, the increasing peak area ratio of $\text{Co}^{2+}/\text{Co}^{3+}$ indicates the higher *Ov* content [24]. Herein, the $\text{Co}^{2+}/\text{Co}^{3+}$ ratio in Co 2p spectra followed the similar trend to that of *Ov*/Co–O ratio of O 1s spectra, *i.e.*, NFZ-5 > NFZ-10 > NFZ-20 > NFZ-Air (Fig. 2b). The presence of *Ov* was further confirmed using Raman spectroscopy (Fig. 2c). All four samples exhibited peaks at $195, 477, 514$, and 678 cm^{-1} , corresponding to $\text{F}_{2g}^{(1)}$, E_g , $\text{F}_{2g}^{(2)}$, and A_1g phonon modes of the spinel structured Co_3O_4 , respectively. The observed peak shift of A_1g (CoO_6 , octahedral sites) could be attributed to lattice contraction/ extension and surface reconstruction because of the surface *Ov* [25]. Meanwhile, half widths of A_1g peaks decreased in the order: NFZ-5 (39 cm^{-1}) > NFZ-10 (32 cm^{-1}) > NFZ-20 (22 cm^{-1}) > NFZ-Air (17 cm^{-1}), suggesting the formation of *Ov*. The *Ov* contents (δ value) of the as-synthesized materials, determined by iodometric titration method, were 0.354, 0.521, 0.687, and 0.912 for NFZ-Air, NFZ-20, NFZ-10 and NFZ-5, respectively (Fig. 2d and Table S3) [26]. The *Ov* content was negatively associated with oxygen pressure, *i.e.*, the higher *Ov* could be generated at the lower oxygen pressure. Overall, these results confirmed the successful preparation of Co_3O_4 -based membranes, in which δ values could be regulated by calcinating the electrochemically synthesized NFZ materials under controlled oxygen atmosphere.

3.3. Catalytic performance of NFZ-derived membranes

The catalytic performance of NFZ-5, NFZ-10, NFZ-20, and NFZ-Air was evaluated based on BPA degradation via PMS activation. Control experiments showed that the contributions of BPA removal from self-decomposition of PMS (~7%, Fig. 3a), BPA adsorption (< 8%, Fig. S7a), and substrate (< 10%, Fig. S7b) were rather limited. However, in presence of NFZ-20 and NFZ-Air, BPA removal efficiency reached 67% and 88%, respectively, within 60 min. In fact, the complete BPA degradation (100%) was attained with the NFZ-5 membrane. The corresponding kinetic rate constant ($k = 0.11 \text{ min}^{-1}$; $R^2 = 0.995$) was found to be 2.5, 3.7, and 5.6 times higher than that obtained with NFZ-10 ($k = 0.045 \text{ min}^{-1}$; $R^2 = 0.998$), NFZ-Air ($k = 0.031 \text{ min}^{-1}$; $R^2 = 0.999$), and NFZ-20 ($k = 0.020 \text{ min}^{-1}$; $R^2 = 0.994$), respectively (Fig. 3a).

The leachable Co from the NFZ-derived membrane was determined to be lesser than that of 10 \mu g/L during reaction. A control experiment by mixing 10 \mu g/L Co^{2+} and 1.5 mM PMS in a homogeneous system only led to the minimal BPA degradation (< 10%) under neutral pH. When the concentration of Co^{2+} increased to 50 \mu g/L , 35% BPA degradation was recorded (the initial Co content of NFZ membrane ($\text{C}_8\text{H}_{10}\text{N}_4\text{Co}$) was 0.995 mg/cm^2 ; Fig. S8). These results ruled out the potential contribution from the activation of PMS by leached Co^{2+} . The BPA removal efficiency of the as-synthesized membrane was also evaluated herein using the commercial grade Co_3O_4 ($400 \pm 100 \text{ nm}$) under similar conditions (Fig. S9). Results showed that degradation rates of NFZ-5, NFZ-10, and NFZ-Air were 4.8, 2.0, and 1.4 times higher, respectively, than that of

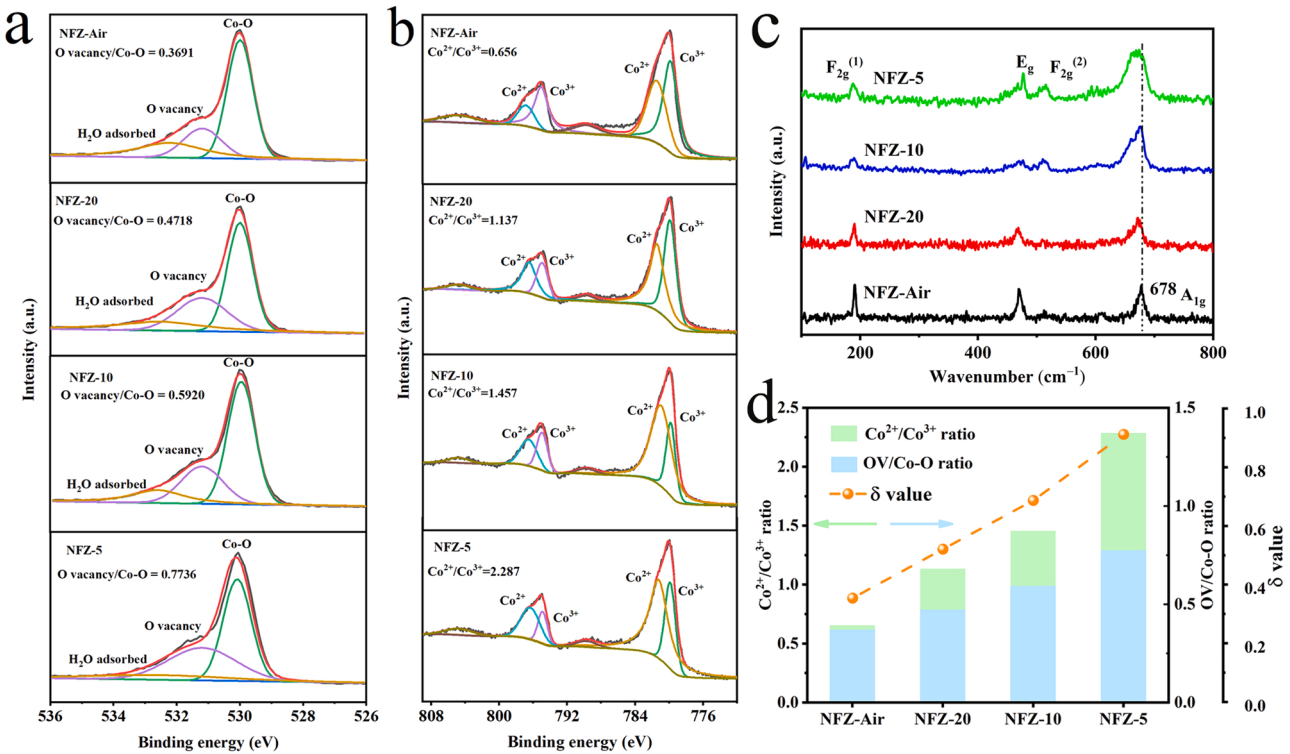


Fig. 2. Ov content characterization of NFZ-Air, NFZ-20, NFZ-10, and NFZ-5 membranes: (a) High resolution XPS O 1s and (b) Co 2p spectra, (c) Raman spectra, (d) Ov/Co-O ratio, $\text{Co}^{2+}/\text{Co}^{3+}$ ratio, and δ value of NFZ-derived catalysts.

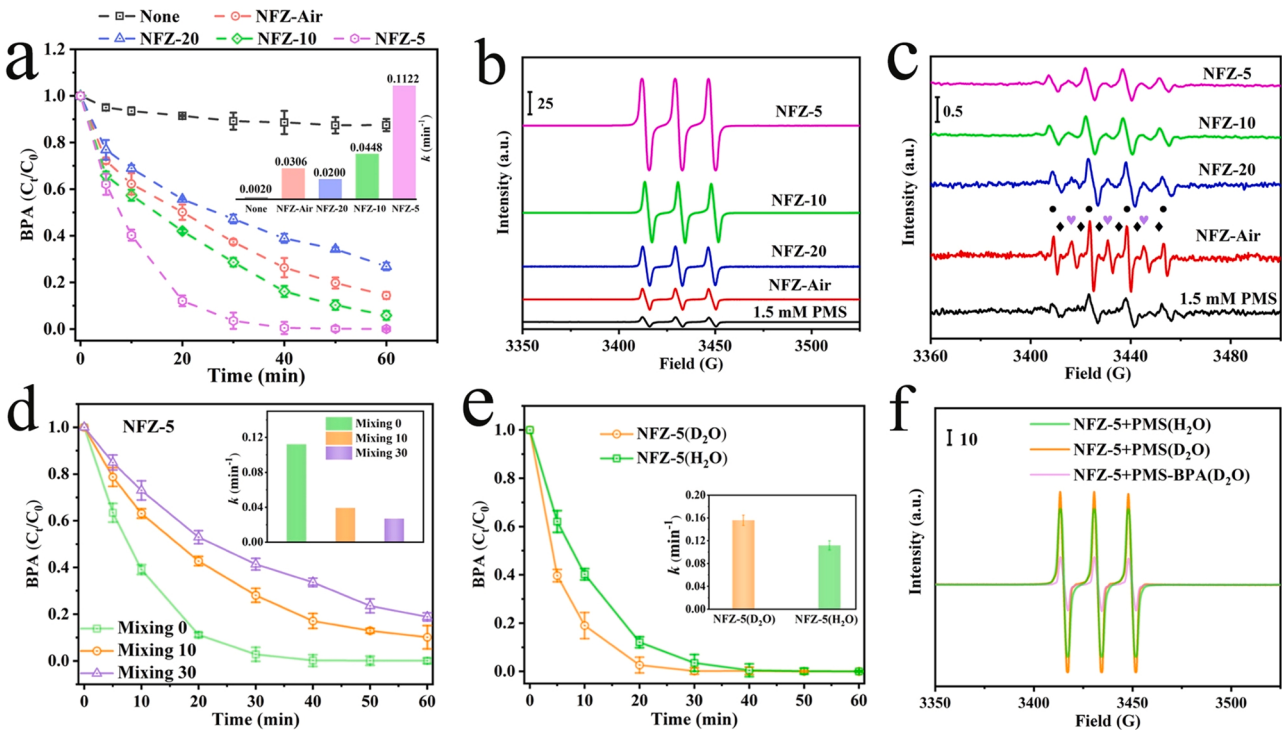


Fig. 3. (a) Degradation performance of each NFZ-derived membrane/PMS system ($[\text{BPA}] = 0.044 \text{ mM}$, $[\text{PMS}] = 1.0 \text{ mM}$, flow rate = 1.5 mL/min); EPR spin-trapping experiments with (b) TEMP and (c) DMPO (\bullet DMPO- HO^{\bullet} , \blacklozenge DMPO- $\text{SO}_4^{\bullet-}$, \heartsuit DMPO-X), respectively; (d) the removal efficiency of BPA after PMS mixing with NFZ-5 in advance (BPA added at 10 and 30 min are labelled as mixing 10 and 30 min, respectively); effect of D_2O on (e) BPA removal efficiency and (f) $\text{TEMP}-\text{O}_2$ signals.

the $\text{Co}_3\text{O}_4/\text{PMS}$ system ($[\text{Co}] = 0.995 \text{ mg/cm}^2$, $k = 0.0228 \text{ min}^{-1}$, $R^2 = 0.989$). The mineralization efficiency (monitored by total organic carbon analysis) of the NFZ-5/PMS system for BPA removal attained 57.1% within 40 min (Fig. S10), demonstrating the efficient catalytic activity of the membrane material. These findings quantitatively exemplified the advantages of the proposed technology toward decontamination of aqueous micropollutants. Although the practical applications of MOF-derived materials for water treatment have been rarely reported, recent advances in nanotechnology may provide promising solutions for this dilemma. With delicate design of fine chemistry involved, the physicochemical properties of MOFs can be well-controlled. Moreover, the recent progress in mass production of MOFs also offers another opportunity to produce advanced MOF-derived materials with well-defined structures, superior stability and affordable cost.

The electron paramagnetic resonance (EPR) spin-trapping technique was used to identify the ROS, generated during PMS activation. Fig. 3b shows that triplet signals, corresponding to $\text{TEMP}^{-1}\text{O}_2$ (1:1:1, $\alpha_N = 16.9 \text{ G}$, and $g = 2.0054$) were detected with all catalysts, and their intensity increased with increasing δ values (i.e., NFZ-5 > NFZ-10 > NFZ-20 > NFZ-Air). The intensity of $\text{TEMP}^{-1}\text{O}_2$ adduct signals in NFZ-5/PMS system was 15 and 13 times higher than that of NFZ-Air/PMS and commercial grade $\text{Co}_3\text{O}_4/\text{PMS}$ systems, respectively (Fig. 3b, and Fig. S11). Conversely, when the $\text{SO}_4^{\bullet-}/\text{HO}^{\bullet}$ trapping agent (DMPO) was introduced, little change in intensities of $\text{DMPO-SO}_4^{\bullet-}/\text{HO}^{\bullet}$ signals were observed for all NFZ-derived membrane/PMS systems (Fig. 3c). However, intensities of $\text{DMPO-SO}_4^{\bullet-}/\text{HO}^{\bullet}$ signals ($\alpha_N = \alpha_H = 14.9 \text{ G}$, and $g = 2.004$), especially $\text{DMPO-SO}_4^{\bullet-}$ adduct, generated by NFZ-Air/PMS system were much stronger than those of Ov-rich membranes/PMS and PMS self-decomposition systems.

Scavenger experiments were employed to determine the variation of dominant ROSSs, generated by activated PMS, and δ value of NFZ-derived membranes. MeOH was used to scavenge radicals typically associated with the PMS activation process (i.e., $\text{SO}_4^{\bullet-}$ and HO^{\bullet}) because of the high affinity towards these species ($k_{\text{SO}_4^{\bullet-}} = 1.2\text{--}2.8 \times 10^9 \text{ M}^{-1}\text{s}^{-1}$; $k_{\text{HO}^{\bullet}} = 1.6\text{--}7.7 \times 10^7 \text{ M}^{-1}\text{s}^{-1}$) [27]. In addition, FFA was used to confirm the presence of O_2^{\bullet} ($k_{1\text{O}_2} = 1.2 \times 10^8 \text{ M}^{-1}\text{s}^{-1}$) [28]. It has been reported that the scavenger (e.g., MeOH and TBA) concentration should be 200–1000 times than that of PMS concentration to affect the complete quenching of free radicals. However, much lower doses were required for O_2^{\bullet} -dominated systems (1–20 times) in this work [29]. The effect of excess amounts of radical scavengers ($M_{\text{MeOH}} = 1000 \text{ mM}$ and $M_{\text{FFA}} = 20 \text{ mM}$) in the as-synthesized membranes toward degradation of BPA is shown in Figs. S12 and S13. With the increase in δ values of the catalysts in each PMS/BPA system, the addition of MeOH displayed a contrasting effect on degradation efficiency. Though the maximum inhibition of BPA degradation (75.4%) could be observed for NFZ-Air/PMS system (k decreased from 0.031 to 0.0035 min^{-1}), yet the NFZ-5/PMS system was affected small (4.5% inhibition; k decreased from 0.11 to 0.080 min^{-1}). Hence, results suggested that $\text{SO}_4^{\bullet-}$ and HO^{\bullet} were the main ROSSs in the NFZ-Air/PMS system. When FFA (indicator of O_2^{\bullet}) was added to the NFZ-derived membrane/PMS/MeOH systems, BPA degradation was progressively inhibited as δ value of each system increased. The inhibition efficiency increased from 16.8% in NFZ-Air (i.e., k decreased from 0.0035 to 0.0012 min^{-1}) to 80.5% of NFZ-5 (i.e., k decreased from 0.0801 to 0.0019 min^{-1}), indicating that the positive contribution of O_2^{\bullet} towards δ value. However, the role of O_2^{\bullet} may be overestimated, since TEMPO (TEMP- O_2^{\bullet} adduct) can also be generated by two electron oxidation of TEMP in presence of O_2 (Fig. S14) [30], and the inhibitive effect of FFA (an indicator of O_2^{\bullet}) could also be because of the electron-transfer mechanism [31]. Therefore, the contribution of O_2^{\bullet} associated with δ values requires careful evaluation.

The incorporation of Ov may facilitate charge transfer via reducing resistance of materials [32], as evidenced by the decrease in resistance of NFZ-derivative membranes with increasing δ values (Fig. S15). Moreover, it has been suggested that organic compounds having ionization potential (IP) lower than that of 9.0 eV may act as electron donors

in a mediated electron transfer process. Herein, since the IP value of BPA was ~ 7.5 , it could behave as an electron donor [33]. For further verification of this observation, a few experiments were carried out by exposing NFZ-5 membrane to PMS solution, followed by the addition of BPA at the specific time. If NFZ-5 mediated electron transfer within PMS and BPA, the mixing of PMS and NFZ-5 in advance should have no significant influence on the removal efficiency of BPA. Conversely, if NFZ-5 activated PMS to generate ROS (e.g., O_2^{\bullet}), then BPA removal efficiency should decrease significantly with the increasing mixing time because of the consumption of PMS and the limited lifetime of ROS (e.g., $\text{O}_2^{\bullet} = 2 \mu\text{s}$). From Fig. 3d, the removal rate of BPA was observed to decrease with the increase in mixing time. When H_2O was replaced with D_2O , significant solvent isotope effect was observed in NFZ-5/PMS system, confirmed from the ~ 10 times increase in O_2^{\bullet} lifetime from $k_{1\text{O}_2/\text{H}_2\text{O}} = 2.5 \times 10^5 \text{ M}^{-1}\text{s}^{-1}$ of H_2O to $k_{1\text{O}_2/\text{D}_2\text{O}} = 1.6 \times 10^4 \text{ M}^{-1}\text{s}^{-1}$ in D_2O . Moreover, the rate constant for BPA degradation in D_2O was 1.4 times higher than that in H_2O (Fig. 3e). As expected, the distinct 1:1:1 triplet signal of $\text{TEMP}^{-1}\text{O}_2^{\bullet}$ adducts in NFZ-5/PMS/ D_2O system was much stronger than those in NFZ-5/PMS/ D_2O /BPA and NFZ-5/PMS/ H_2O systems (Fig. 3f). These cumulative evidences inferred the prevalence and significant contribution of O_2^{\bullet} towards to BPA degradation in NFZ-5/PMS system.

To further validate the existence of O_2^{\bullet} and reveal its selective association with δ values, experiments were carried out to quantitatively determine reactive species generated in NFZ-derived membrane/PMS and commercial $\text{Co}_3\text{O}_4/\text{PMS}$ system after addition of different probe molecules [34,35]. Notably, O_2^{\bullet} was detected in all systems, and its population increased with increasing δ values, in which NFZ-5 ($\delta = 0.915$) possessed the highest content (98.3%; Fig. S16). Conversely, the concentrations of $\text{SO}_4^{\bullet-}$ and HO^{\bullet} decreased with the increase in δ values, and NFZ-Air ($\delta = 0.354$) exhibiting the highest radical concentrations ($\text{SO}_4^{\bullet-} = 23.5\%$, $\text{HO}^{\bullet} = 58.7\%$). The rate constants (k) for reactions within BPA and $\text{HO}^{\bullet}/\text{SO}_4^{\bullet-}/\text{O}_2^{\bullet}$ were as follow the trend: $k_{\text{HO}^{\bullet}, \text{BPA}} = 1.70 \times 10^{10} \text{ M}^{-1}\text{s}^{-1}$, $k_{\text{SO}_4^{\bullet-}, \text{BPA}} = 1.37 \times 10^9 \text{ M}^{-1}\text{s}^{-1}$, and $k_{1\text{O}_2, \text{BPA}} = 2.0 \times 10^8 \text{ M}^{-1}\text{s}^{-1}$ [36,37]. Hence, both Ov levels and ROS rate constants determined BPA removal efficiencies, envisaging the higher removal efficiency of NFZ-Air/PMS system than that of NFZ-20/PMS system (Fig. 3a). Till date, a few researchers reported the use of MOFs-derived materials to activate PMS for degradation of micropollutants (Table S2). Among those, interfacial cross-linking and encapsulation strategies were employed by the groups of Lu and Xie for fabricating ZIF-67-derived nanofibrous and ultrafiltration catalysis membranes, respectively [38,39]. The combination of MOF-derived catalysts and membranes technology strongly promoted mass transfer and mitigated the environmental impact, thereby achieving the excellent removal of contaminants. Besides, Zhao and Xu groups introduced Ov on MOF-derived metal oxides (ZnCoO_x and $\alpha\text{-Fe}_2\text{O}_3\text{-x}$) by incorporating additional precursor (metal ions or ligand) to extract oxygen from the neighboring oxygenated lattice during calcination [40,41]. Compared to these reported literatures, the as-synthesized NFZ-derived membranes integrated membrane technology and defect engineering. For this reason, NFZ membrane was synthesized by using electrochemical method allowing the *in-situ* growth of ZIF-67 on Ni-foam without using crosslinkers and encapsulants. Moreover, Ov levels in the host lattice were controlled by varying oxygen pressure during calcination process without using additional precursor, which further reduced production cost. More importantly, the dominant ROS generated during PMS activation could be adjusted by the Ov level of NFZ-derived membranes. Therefore, the as-synthesized catalyst systems exhibit versatility towards a wide range of micropollutants remediation.

Previous studies indicated that $\text{O}_2^{\bullet-}$ could be an intermediate during generation of O_2^{\bullet} via transition metal-mediated PMS activation [42]. Therefore, carbonate (CO_3^{2-}) was selected herein to scavenge $\text{O}_2^{\bullet-}$ ($k = 5 \times 10^8 \text{ M}^{-1}\text{s}^{-1}$) in the NFZ-5/PMS system. The results given in Fig. S17a showed that BPA degradation efficiency was scarcely affected by the addition of 10 mM CO_3^{2-} over the course of the reaction, although

EPR signal confirmed the presence of a DMPO- $\text{O}_2^{\bullet-}$ adduct (Fig. S17b). This phenomenon could be explained by the lower oxidative capability of $\text{O}_2^{\bullet-}$ ($E = -0.33$ V vs normal hydrogen electrode, NHE). Furthermore, BPA removal efficiencies were found to decrease to only $\sim 50\%$ and $\sim 10\%$ because of the addition of 0.1 and 5.0 mM FFA, respectively, in presence of CO_3^{2-} . These results envisaged the non-involvement of $\text{O}_2^{\bullet-}$ during $^1\text{O}_2$ generation. Moreover, experiments performed by pre-saturating reaction solvents with N_2 and O_2 had negligible impact on the degradation of BPA in the NFZ-5/PMS system, that further confirmed the non-generation of $\text{O}_2^{\bullet-}$ from dissolved oxygen to evolve $^1\text{O}_2$ (Fig. S18).

3.4. Surface properties-activity relationship

The surface properties of transition metal oxides play the pivotal role towards their catalytic performance. Among these properties, surface acidity and the nature of surface acidic sites pose the strong influence on catalytic activity [43,44]. Consequently, surface acidities of NFZ-5 and NFZ-Air were characterized by using the temperature-programmed desorption of ammonia (NH_3 -TPD, Fig. 4a and Table S4). Herein, the NH_3 desorption peak at 197.4 °C (desorbed NH_3 concentration was 0.254 mmol/g) in NFZ-Air was attributed to Brønsted acidic sites (< 300 °C). However, in NFZ-5, two desorption peaks at 401.8 °C and

539.1 °C (desorbed NH_3 concentrations were 0.173 mmol/g and 0.133 mmol/g, respectively) envisaged the prevalence of Lewis acid sites (> 300 °C) and the inherently weak acid sites at ~ 196.6 °C (desorbed NH_3 concentration was 0.11 mmol/g). These results indicated that the higher δ value (0.915) of NFZ-5 represented the larger number of Lewis acidic sites on the surface of NFZ-5 membrane.

For further rationalization of this, pyridine FTIR spectroscopy was used to analyze the changes in surface acidity on NFZ-5 and NFZ-Air, before and after the PMS-activated degradation of BPA. Herein, peaks at 1447 and 1598 cm^{-1} were assigned to the interaction of pyridine with Lewis acidic sites, whereas peaks at 1540 and 1490 cm^{-1} were attributed to interactions within pyridine and Brønsted acidic sites and adsorbed pyridine on both types of acidic sites, respectively. Previous studies concerning surface acidity sites in transition metal oxides have generally referred to Ov sites and the incorporation of water molecules [45]. From Fig. 4b, Fig. S19 and Table S5, the proportion of Lewis acidic sites to Brønsted acidic sites was found to be much higher in NFZ-5 (24.8) than that in NFZ-Air (8.20). Quantification of the Lewis acidic sites in NFZ-5 system inferred the decrease in initial concentration (17.0 $\mu\text{mol/g}$) after reaction (12.2 $\mu\text{mol/g}$), envisaging the major activation characteristics of Lewis acidic sites (Ov) in the catalyst system.

In situ Raman and ATR-FTIR were used to monitor the evolution of surface chemistry of NFZ-Air and NFZ-5 during activation of PMS. In

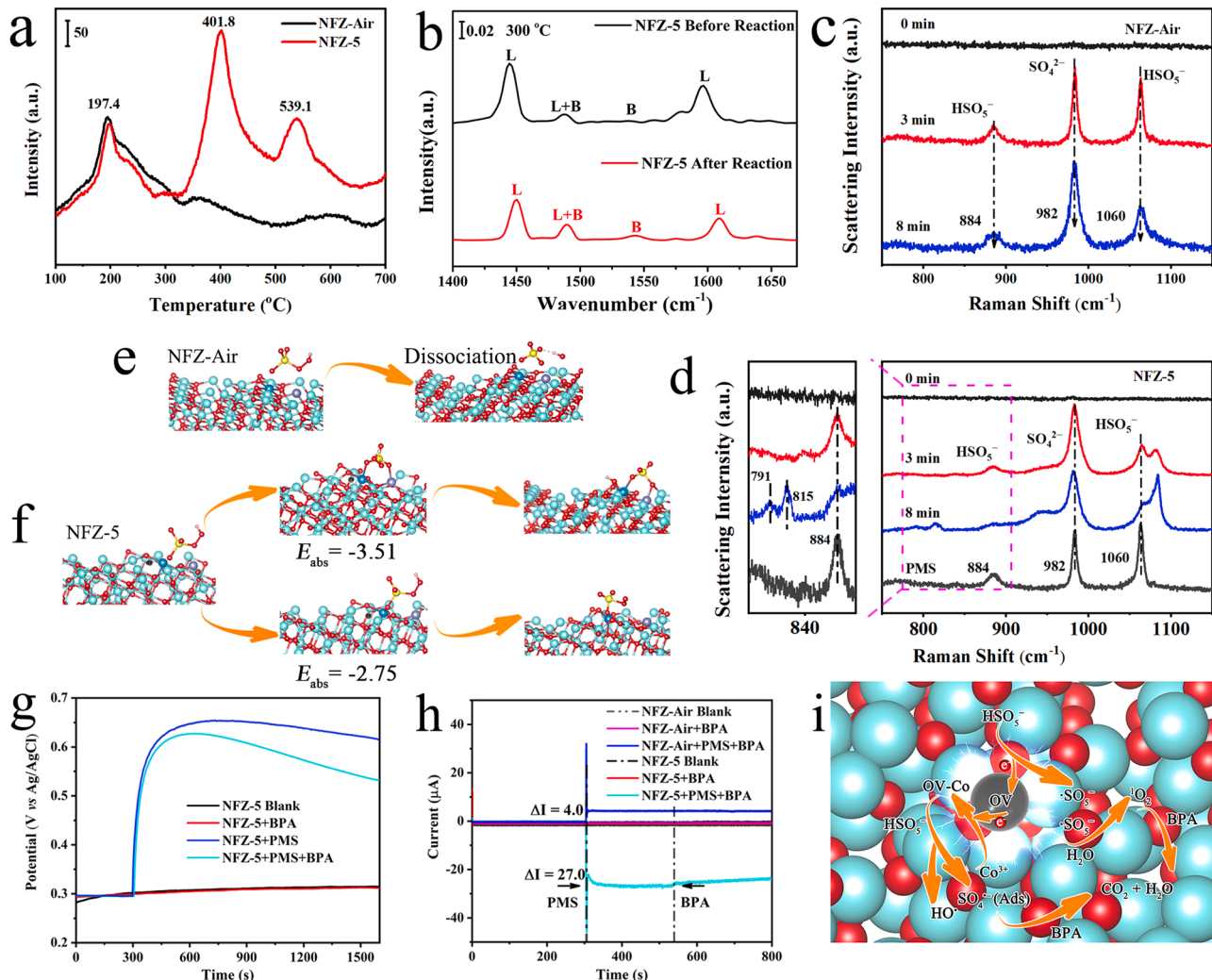


Fig. 4. Surface property-activity relationships: (a) NH_3 -TPD profiles of NFZ-5 and NFZ-Air; (b) pyridine FTIR spectra of the pristine and used NFZ-5; *in situ* Raman spectroscopy of PMS (HSO_5^-) in (c) NFZ-Air and (d) NFZ-5 systems; DFT optimized geometry of the PMS molecule on the surface of (e) NFZ-Air and (f) NFZ-5; (g) open-circuit potential curves of the NFZ-5 electrodes after the addition of PMS and BPA; (h) charge migration during the activation of PMS and oxidation of BPA with the NFZ-5 and NFZ-Air systems; (i) proposed mechanisms of BPA decomposition in the NFZ-5/PMS system.

Raman spectrum of PMS, peaks at 881 and 978/ 1060 cm^{-1} were assigned to O–O str. of HSO_5^- and S=O sym. str. of SO_4^{2-} / HSO_5^- , respectively. Radical generation in NFZ-Air/PMS system *via* transformation of HSO_5^- into SO_4^{2-} was further confirmed by the significant increase in peak intensity at 982 cm^{-1} relative to the neighboring peak at 1060 cm^{-1} (Fig. 4c). This was also consistent with the ATR-FTIR results (Fig. S20), leading to a minor shift of the O-lattice peak towards the higher frequency after reaction (Fig. S21). Importantly, in the Raman spectrum of NFZ-5/PMS system, the generation of a shoulder at 1080 cm^{-1} after 3 min of reaction time envisaged the coexistence of PMS (HSO_5^-) in two different forms on the surface of NFZ-5 initially. After 8 min of reaction, arrival of two new peaks at 791 and 815 cm^{-1} (Fig. 4d) was assigned to the formation of two types of highly reactive peroxy species (labeled PMS*) [46–48]. In addition, compared to the peaks in Raman spectrum of PMS system, intensity of the peak at 884 cm^{-1} because of $\text{HO}-\text{OSO}_3^-$ reduced significantly, while the peak of S=O (1060 cm^{-1} in PMS system) red shifted to 1080 cm^{-1} in NFZ-5. These observations indicated the prevalence of strong interactions within O–O band of $\text{HO}-\text{OSO}_3^-$ and active Lewis acidic sites in NFZ-5/PMS system.

DFT calculations were used to further understand the interactions within PMS and the active sites of NFZ-5. A Co_3O_4 (311) slab model was considered to represent the exposed surface of the catalyst based on its highest intensity in XRD spectra (Fig. 1m). The results confirmed that in NFZ-Air system, PMS was spontaneously decomposed into SO_4^{2-} and HO^\bullet on the surface of the catalyst (Fig. 4e), which was consistent with the previous experimental results. In the NFZ-5 system, PMS was preferentially chemisorbed onto the unsaturated coordinated Co site ($E_{\text{ads}} = -3.51$ eV) and Ov ($E_{\text{ads}} = -2.75$ eV), suggesting the formation of surface-confined complexes (i.e., Co-PMS* and Ov-PMS*). The Co-PMS* then transformed into the surface bonded SO_4^{2-} radicals, whereas Ov-PMS* evolved into SO_5^- without any energy barrier (Fig. 4f). Because of the high reaction rate ($k \approx 2 \times 10^8 \text{ M}^{-1} \text{ s}^{-1}$) and low activation energy ($7.4 \pm 2.4 \text{ kcal mol}^{-1}$) [49], self-reaction of SO_5^- occurred rapidly leading to the formation of ${}^1\text{O}_2$, SO_4^- , and $\text{S}_2\text{O}_8^{2-}$ (Fig. 4d and f, Eqs. 1–3).



Subsequently, KI and PMSO were used to confirm the involvement of surface-bound radicals and metastable high-valence metal intermediates (Co(IV)) in the activation process, respectively. The addition of 10 mM KI reduced the degradation efficiency of BPA to 76.7% (Fig. S22), demonstrating the partial decomposition of BPA *via* reaction with surface-bound radicals/ complexes derived from activated PMS. Herein, obsolescence of the signals corresponding to PMSO₂ in the HPLC spectrum suggested the non-formation of high-valent Co-intermediates in NFZ-5/PMS system (Fig. S23).

Although Ov appeared to play the key role during nonradical activation of PMS in NFZ-5/PMS/BPA system, the mechanism of electron transfer was still unclear. Chronopotentiometry is a powerful technique frequently used to study redox mechanism. Here, it was used to elicit the potentials of Ov-enriched NFZ-5 and Ov-deficient NFZ-Air systems after addition of PMS/BPA. After PMS addition, the potential of NFZ-5 system increased initially from 0.295 to 0.652 V (vs Ag/AgCl), after which the reverse trend was observed (Fig. 4g). The entire variation was found to occur more rapidly in presence of BPA. The addition of PMS and BPA had minor effect on the potentials of NFZ-Air and Ni-foam systems (Fig. S24). Presumably, the activation of PMS to form PMS* intermediates in NFZ-5/PMS system elevated the measured electrode potential, followed by decreasing because of the dissociation of surface bonded PMS. Notably, the decrease in potential was more

evident in presence of BPA (Fig. S25). To further understand these results, chronoamperometry was employed to monitor charge migration during PMS activation and the oxidative degradation of BPA. Fig. 4h showed that there was no appreciable difference in the measured currents obtained at equilibrium potentials of NFZ-5 (+0.29 V) and NFZ-Air (+0.24 V) with and without added BPA (0.044 mM). However, when PMS (1.0 mM) was injected into the NFZ-5-based three-electrode system, current decreased immediately ($\Delta I = 27.0 \mu\text{A}$), and remained stable following the subsequent addition of BPA. However, the current in NFZ-Air-based three-electrode system increased ($\Delta I = 4.0 \mu\text{A}$) after the addition of PMS. Such observation suggested that Ov-enriched NFZ-5 acted as an electron acceptor resulting in the oxidation of PMS to generate SO_5^- , which then triggered the predominantly ${}^1\text{O}_2$ based non-radical degradation of BPA [50]. Conversely, electrons were donated to PMS in the NFZ-Air system, which facilitated the O–O cleavage of PMS to generate SO_4^- and HO^\bullet .

3.5. Proposed mechanism of NFZ-5/PMS activated BPA degradation

Associated with the Ov fingerprint (Fig. 2a, b, XPS spectra; Fig. 2c Raman spectra), the stronger signal of $\text{TEMP}-{}^1\text{O}_2$ adducts and elevated BPA degradation when D_2O was employed as a solvent (Fig. 3b-f), and the increased the Lewis acidic sites (Fig. 4a, b; Table S5). Hence, the presence of Ov in NFZ-5 was confirmed to be the primary requisite for producing ${}^1\text{O}_2$ by activating PMS. In conjunction with DFT calculations and electrochemical analyses, a dual-reaction-site mechanism was proposed for the oxidation of BPA in NFZ-5/PMS system (Fig. 4i) that comprised of (i) adsorption of PMS onto the single electron-trapped Ov sites and unsaturated coordinated Co sites to form metastable Ov-PMS* and Co-PMS*intermediates (Fig. 4d and f, *in-situ* Raman and DFT calculation); (ii) elevation of the potential of activated complex of NFZ-5 (Fig. 4g), followed by oxidation of Ov-PMS* to SO_5^- *via* transferring electron to Ov, and the rapid self-reaction process of SO_5^- triggering ${}^1\text{O}_2$ dominated non-radical BPA degradation pathway; and (iii) possibility of the formation of surface-bound SO_4^- from Co-PMS* intermediates that in conjunction with ROS (${}^1\text{O}_2$ dominated) was immediately consumed by BPA to accelerate the electron accumulation and depletion for completing a catalytic cycle (Fig. S26, the $\text{Co}^{2+}/\text{Co}^{3+}$ peak area ratios in Co 2p exhibited a slight decrease and the binding energy of O lattice associated with Ov of the catalyst showed no differences before and after the catalytic reaction). In conjunction with the PMS activation mechanism of NFZ-5/PMS and NFZ-Air/PMS systems, the possible oxidation pathways of BPA were investigated by its degradation intermediates (identified by LC–MS) and previous studies [51], the results are given in Figs. S27 and S28.

Herein, the potential of the Ov-enriched NFZ-5 membrane activated PMS system towards detoxification of the generated intermediates was also essential, since these degradation products might be more deleterious than that of BPA. Hence, the ecotoxicity inducing acute toxicity (Fathead minnow), bioaccumulation factor, developmental toxicity, and mutagenicity of BPA and reaction intermediates (Ov-deficient NFZ-Air system: A~K, Fig. S27; Ov-enriched NFZ-5 system: O~T, Fig. S28) were compared by quantitative structure–activity relationship (QSAR) prediction by using the Toxicity Estimation Software (T.E.S.T.) [52]. As displayed in Fig. 5a, the LC₅₀ (96 h) of fathead minnow was 4.65 mg/L for BPA, categorized as “Toxic”. Interestingly, the acute toxicities of products generated from NFZ-5 system were significantly lower, even the product Q was found to be “Not harmful” ($> 1000 \text{ mg/L}$) compared with those of NFZ-Air system. Fig. 5b exhibited that Ov-enriched NFZ-5/PMS system could decrease the bioaccumulation factor of most reaction intermediates (< 24.51). For instance, the bioaccumulation factors of intermediates O, P, Q, R, and S decreased by 34.1%, 84.8%, 95.9%, 85.5%, and 45.2%, respectively, compared to that of BPA. Moreover, BPA is a “developmental toxicant”, while the oxidation process reduces the toxicity of degradation products, this phenomenon is especially obvious in NFZ-5/PMS based oxidation process (products

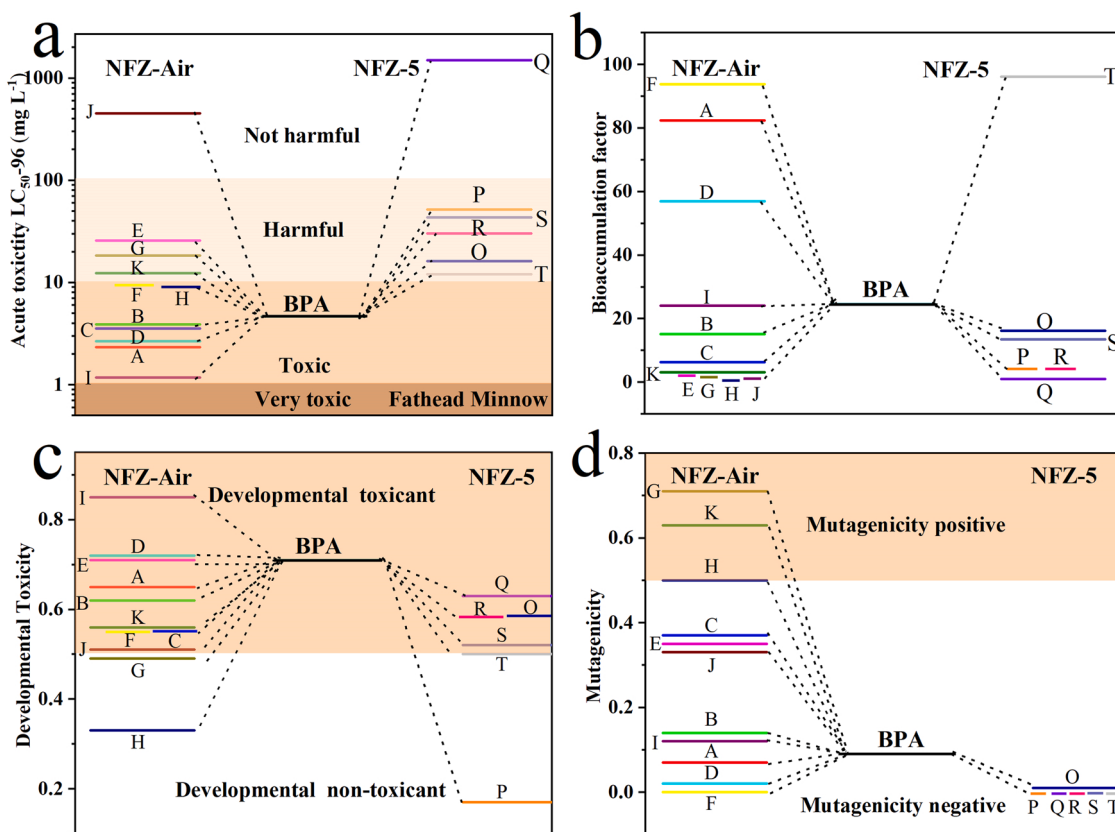


Fig. 5. (a) Acute toxicity (Fathead minnow), (b) bioaccumulation factor, (c) developmental toxicity and (d) mutagenicity of BPA and its degradation intermediates in NFZ-Air/PMS and NFZ-5/PMS systems.

O~T, Fig. 5c). Fig. 5d suggested that oxidation reaction present in NFZ-5 system also reduced the mutagenicity of these products to the lower “mutagenicity negative” status, which was more favorable than that of BPA (0.09). From the calculated results, the constructed Ov-enriched NFZ-5/PMS system not only removed BPA effectively, but also further attenuated the comprehensive toxicity of BPA compare with NFZ-Air/PMS system.

3.6. Practical application

Since ${}^1\text{O}_2$ is reported to be a selective oxidant for organic pollutants, the NFZ-5/PMS system was expected to demonstrate optimum performance in complex water matrices. To confirm this, the efficacy of the NFZ-5/PMS degradation system was challenged using different refractory pollutants, such as erioglaucine disodium salt (EDS), tetracycline (TC), sulfamethoxazole (SMX), BPA, phenol, and benzoic acid, (Table S6) under various operating conditions, such as pH, coexisting anions, and natural organic matter. Fig. 6a revealed that the NFZ-5/PMS system enabled effective degradation of the electron-rich contaminants. The degradation of benzoic acid was limited by its mild oxidation capability (2.2 eV vs NHE) and electrophilic oxidation mechanism of ${}^1\text{O}_2$.

Inorganic anions, such as SO_4^{2-} , Cl^- , HPO_4^{2-} and HCO_3^{2-} , and natural organic matter, such as humic acids, are ubiquitous in natural water resources that may interfere the oxidative removals of micropollutants. From Fig. 6b, the addition of SO_4^{2-} , Cl^- , HPO_4^{2-} (1–10 mM), and humic acid (1–20 mg/L) had negligible effects on BPA removal efficiency. However, the introduction of HCO_3^{2-} decreased the degradation efficiency of BPA from 97.3% at 1 mM of HCO_3^{2-} to 89.7% in 10 mM of HCO_3^{2-} within 60 min because of the reaction of HCO_3^- with the surface-bonded radicals, replicating the characteristics of a scavenger, such as Cl^- . However, the generated carbonate radicals possessed the lower

redox potentials than those of reactive chlorine radicals [53,54]. Solution pH is also an important factor affecting the PMS activation process. From Fig. 6c, the efficiency of NFZ-5-catalyzed PMS activation system was found to increase significantly with the increase in pH because of the different speciation of PMS at variable pH conditions [55].

Reusability of the NFZ-5/PMS system is important for sustained practical application. The results obtained from an extended cycling test showed that the BPA degradation performance of NFZ-5/PMS system decreased slightly after four consecutives cycles (~90%, Fig. 6d). Since, BPA oxidation intermediates might accumulate and occupy the active sites (Fig. S26), the exhausted membrane was irradiated (Xe, 320–780 nm) to remove surface remnants to reactivate the passivated sites, as evidenced by the restored BPA degradation efficiency after irradiation treatment (Fig. 6d). Fig. S29 showed that the dissolution of Co during cycling tests was much lower than the regulated standards for surface water ($[\text{Co}] < 1.0 \text{ mg/L}$), and the total leachable Co over 9 consecutive cycles (3.55 μg) was only 0.5% of the initial Co (7.06 mg). To further assess the practical applications of these catalytic membranes, the system was treated with lake water (98.8%, $k = 0.092 \text{ min}^{-1}$) and actual pharmaceutical wastewater (91.2%, $k = 0.042 \text{ min}^{-1}$) spiked with BPA of similar concentration. The results showed that different water matrices had negligible effect on BPA removal demonstrating the high selectivity and performance of the proposed technology (Fig. S30). These encouraging results strongly confirmed the robustness of the NFZ-5/PMS system toward decontamination of micropollutants from different water matrices. In addition, XRD patterns and SEM images of the used NFZ-5 catalyst showed no differences in their crystal structure and surface topography, respectively (Figs. S31 and S32).

Table S7 compares the catalytic activity of NFZ-derived membranes with various conventional catalysts for activation of PMS at room temperature. It can be found that NFZ-derived membranes, especially NFZ-5

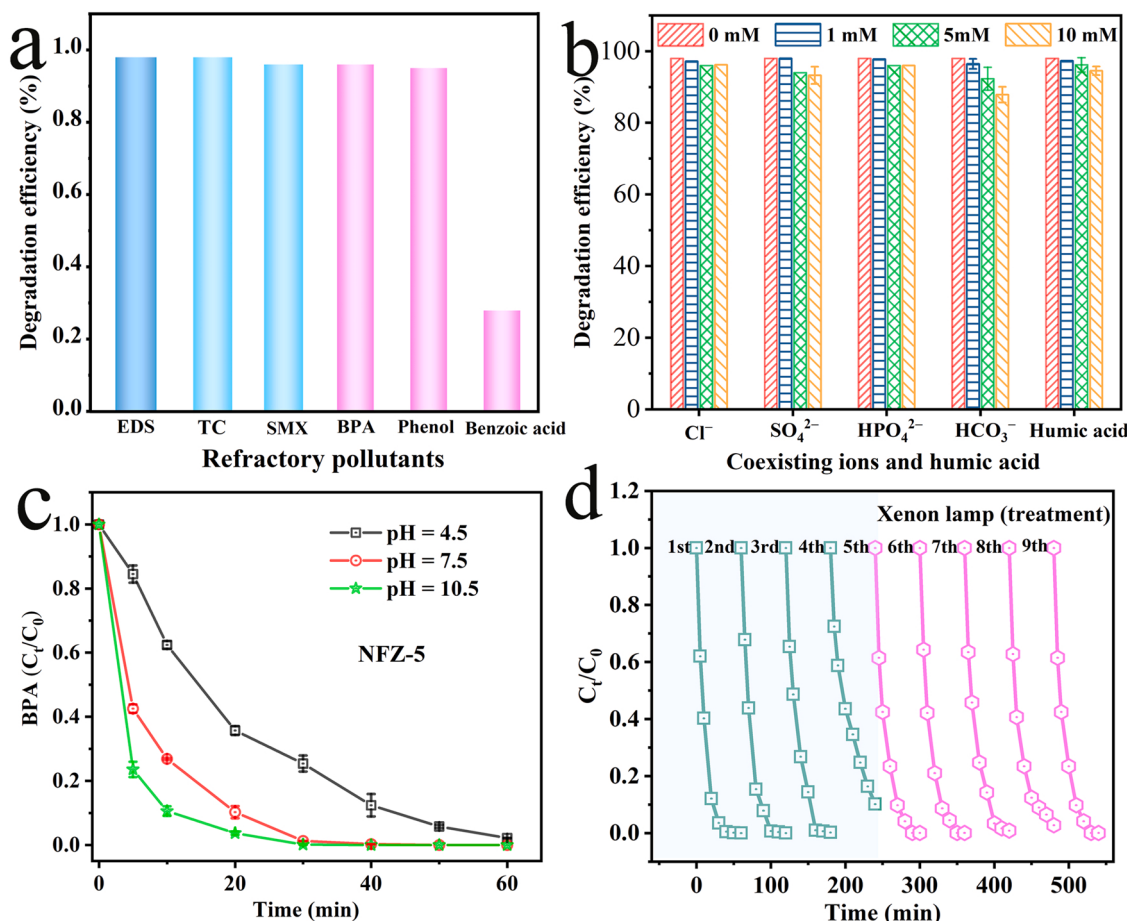


Fig. 6. (a) Degradation efficiency towards different refractory pollutants ($[EDS, TC, SMX] = 20 \text{ mg/L}$, $[BPA, \text{phenol, benzoic acid}] = 10 \text{ mg/L}$), (b) BPA degradation efficiency in presence of various inorganic anions and humic acid; (c) effect of initial pH on the BPA removal in NFZ-5/PMS system, (d) recycling test of the NFZ-5/PMS system ($[BPA] = 10 \text{ mg/L}$, $[PMS] = 0.5 \text{ mM}$, flow rate = 1.5 mL/min ; membrane cleaned by irradiation (Xe, $320 - 780 \text{ nm}$).

demonstrated the superiorities in short degradation time (30 min), high removal efficiency (98%), and fast degradation rate (1.24 L/g-min , normalized by effective mass). According to the characteristics of wastewater and treatment requirements, the as-synthesized NFZ-driven membrane/PMS system could selectively generate ROS by flexibly manipulating the O_v level during calcination process, achieving the most efficient utilization of PMS. Moreover, flow-through design featured with the convection-enhanced mass transport, which favored to overcome the limitations associated with poor mass transport kinetics in conventional batch chemistry.

4. Conclusions

Herein, a series of NFZ-derived membranes with fine-tune O_v have been rationally designed and demonstrated toward the removals of micropollutants by PMS activation. The O_v level can be tailored by controlling the pressure of oxygen atmosphere during calcination. The NFZ-5 with the largest O_v content has shown the highest $^{1}\text{O}_2$ yield as well as the fastest BPA degradation kinetics. Experimental characterization and DFT calculations have collectively verified the essential role of O_v in increasing the surface *Lewis* acidic sites and facilitating chemisorption of PMS. The superior system efficacy can be maintained across a wide range of solution pH and different water matrices. The findings from this study may advance the rational design of next-generation MOF-based catalysts via defect engineering toward effective and selective removal of electron-rich micropollutants from water systems. Nonetheless, there are numerous challenges associated with MOF-based materials in practical applications, especially their production costs. The

price is anticipated to be reduced by the development of newly optimized green procedures, such as mechanochemistry and continuous-flow chemistry synthesis, to replace the traditional solvothermal approach and manipulating amounts and types of raw materials, such as solvent, organic ligand, and metal source). We believe that MOF-based materials would extend this field and broaden the scope of applications related to society with large-scale, interdisciplinary/multi-site collaborations.

CRediT authorship contribution statement

Mohua Li: Conceptualization, Investigation, Writing – original draft. **Shijie You:** Supervision, Project administration. **Xiaoguang Duan:** Formal analysis. **Yanbiao Liu:** Supervision, Writing – review & editing, Funding acquisition.

Declaration of Competing Interest

The authors declare that they have no known competing financial interests or personal relationships that could have appeared to influence the work reported in this paper.

Acknowledgements

This work is supported by the National Natural Science Foundation of China (No. U21A20161 and 52170068), and Open Project of State Key Laboratory of Urban Water Resource and Environment, Harbin Institute of Technology (No. QAK202108).

Appendix A. Supporting information

Supplementary data associated with this article can be found in the online version at doi:10.1016/j.apcatb.2022.121419.

References

- [1] A. Alsbaei, B.J. Smith, L. Xiao, Y. Ling, D.E. Helbling, W.R. Dichtel, Rapid removal of organic micropollutants from water by a porous beta-cyclodextrin polymer, *Nature* 529 (2016), 190-U146.
- [2] U. von Gunten, Oxidation processes in water treatment: Are we on track, *Environ. Sci. Technol.* 52 (2018) 5062–5075.
- [3] Y. Liu, G. Gao, C.D. Vecitis, Prospects of an electroactive carbon nanotube membrane toward environmental applications, *Acc. Chem. Res.* 53 (2020) 2892–2902.
- [4] X.T. Li, J. Wang, X.G. Duan, Y. Li, X.B. Fan, G.L. Zhang, F.B. Zhang, W.C. Peng, Fine-tuning radical/nonradical pathways on graphene by porous engineering and doping strategies, *ACS Catal.* 11 (2021) 4848–4861.
- [5] D. Huang, G. Zhang, J. Yi, M. Cheng, C. Lai, P. Xu, C. Zhang, Y. Liu, C. Zhou, W. Xue, R. Wang, Z. Li, S. Chen, Progress and challenges of metal-organic frameworks-based materials for SR-AOPs applications in water treatment, *Chemosphere* 263 (2021), 127672.
- [6] S. Waclawek, H.V. Lutze, K. Grubel, V.V.T. Padil, M. Cernik, D.D. Dionysiou, Chemistry of persulfates in water and wastewater treatment: a review, *Chem. Eng. J.* 330 (2017) 44–62.
- [7] J. Wang, S. Wang, Activation of persulfate (PS) and peroxymonosulfate (PMS) and application for the degradation of emerging contaminants, *Chem. Eng. J.* 334 (2018) 1502–1517.
- [8] Q. Ji, L. Bi, J. Zhang, H. Cao, X.S. Zhao, The role of oxygen vacancies of ABO(3) perovskite oxides in the oxygen reduction reaction, *Energy Environ. Sci.* 13 (2020) 1408–1428.
- [9] M. Li, P. Wang, Z. Ji, Z. Zhou, Y. Xia, Y. Li, S. Zhan, Efficient photocatalytic oxygen activation by oxygen-vacancy-rich CeO₂-based heterojunctions: Synergistic effect of photoexcited electrons transfer and oxygen chemisorption, *Appl. Catal. B Environ.* 289 (2021), 120020.
- [10] F. Chen, Z. Ma, L. Ye, T. Ma, T. Zhang, Y. Zhang, H. Huang, Macroscopic spontaneous polarization and surface oxygen vacancies collaboratively boosting CO₂ photoreduction on BiOIO₃ single crystals, *Adv. Mater.* 32 (2020), 1908350.
- [11] W. Gao, S. Li, H. He, X. Li, Z. Cheng, Y. Yang, J. Wang, Q. Shen, X. Wang, Y. Xiong, Y. Zhou, Z. Zou, Vacancy-defect modulated pathway of photoreduction of CO₂ on single atomically thin AgInP₂S₆ sheets into olefiant gas, *Nat. Commun.* 12 (2021) 4747.
- [12] H. Abe, A. Murakami, S. Tsunekawa, T. Okada, T. Wakabayashi, M. Yoshida, M. Nakayama, Selective catalyst for oxygen evolution in neutral brine electrolysis: an oxygen-deficient manganese oxide film, *ACS Catal.* 11 (2021) 6390–6397.
- [13] P. Wang, X. Li, S. Fan, X. Chen, M. Qin, D. Long, M.O. Tad, S. Liu, Impact of oxygen vacancy occupancy on piezo-catalytic activity of BaTiO₃ nanobelts, *Appl. Catal. B Environ.* 279 (2020), 119340.
- [14] Y.C. Wang, J.M. Wu, Effect of controlled oxygen vacancy on H₂ production through the piezocatalysis and piezophotonics of ferroelectric R3C ZnSnO₃ nanowires, *Adv. Funct. Mater.* 30 (2020), 1907619.
- [15] K. Zhu, F. Shi, X. Zhu, W. Yang, The roles of oxygen vacancies in electrocatalytic oxygen evolution reaction, *Nano Energy* 73 (2020), 104761.
- [16] Y. Bu, H. Li, W. Yu, Y. Pan, L. Li, Y. Wang, L. Pu, J. Ding, G. Gao, B. Pan, Peroxydisulfate activation and singlet oxygen generation by oxygen vacancy for degradation of contaminants, *Environ. Sci. Technol.* 55 (2021) 2110–2120.
- [17] J.H. Lim, M.R. Hoffmann, Peroxymonosulfate (PMS) activation on cobalt-doped TiO₂ nanotubes: degradation of organics under dark and solar light irradiation conditions, *Environ. Sci.: Nano* 7 (2020) 1602–1611.
- [18] J. Lim, Y. Yang, M.R. Hoffmann, Activation of peroxymonosulfate by oxygen vacancies-enriched cobalt-doped black TiO₂ nanotubes for the removal of organic pollutants, *Environ. Sci. Technol.* 53 (2019) 6972–6980.
- [19] M. Li, M. Dinca, Reductive electrosynthesis of crystalline metal-organic frameworks (N), *J. Am. Chem. Soc.* 133 (2011) 12926–12929.
- [20] B. Tansel, J. Sager, T. Rector, J. Garland, R.F. Strayer, L. Levine, M. Roberts, M. Hummerick, J. Bauer, Significance of hydrated radius and hydration shells on ionic permeability during nanofiltration in dead end and cross flow modes, *Sep. Purif. Technol.* 51 (2006) 40–47.
- [21] Z. Jiang, G. Xu, Z. Yu, T. Zhou, W. Shi, C. Luo, H. Zhou, L. Chen, W. Sheng, M. Zhou, L. Cheng, R.S. Assary, S. Sun, K. Amine, H. Sun, High rate and long cycle life in Li-O₂ batteries with highly efficient catalytic cathode configured with Co₃O₄ nanoflower, *Nano Energy* 64 (2019), 128312.
- [22] R. Das, P. Pachfule, R. Banerjee, P. Poddar, Metal and metal oxide nanoparticle synthesis from metal organic frameworks (MOFs): finding the border of metal and metal oxides, *Nanoscale* 4 (2012) 591–599.
- [23] D.M. Fernandes, P. Mathumba, A.J.S. Fernandes, E.I. Iwuoha, C. Freire, Towards efficient oxygen reduction reaction electrocatalysts through graphene doping, *Electrochim. Acta* 319 (2019) 72–81.
- [24] L. Zhuang, L. Ge, Y. Yang, M. Li, Y. Jia, X. Yao, Z. Zhu, Ultrathin iron-cobalt oxide nanosheets with abundant oxygen vacancies for the oxygen evolution reaction, *Adv. Mater.* 29 (2017), 1606793.
- [25] J.Z. Huang, H.Y. Sheng, R.D. Ross, J.C. Han, X.J. Wang, B. Song, S. Jin, Modifying redox properties and local bonding of Co₃O₄ by CeO₂ enhances oxygen evolution catalysis in acid, *Nat. Commun.* 12 (2021) 3036.
- [26] D. Liu, C. Zhang, Y. Yu, Y. Shi, Y. Yu, Z. Niu, B. Zhang, Hydrogen evolution activity enhancement by tuning the oxygen vacancies in self-supported mesoporous spinel oxide nanowire arrays, *Nano Res.* 11 (2018) 603–613.
- [27] X. Zhou, Q. Zhao, J. Wang, Z. Chen, Z. Chen, Nonradical oxidation processes in PMS-based heterogeneous catalytic system: generation, identification, oxidation characteristics, challenges response and application prospects, *Chem. Eng. J.* 410 (2021), 128312.
- [28] W.T. Zhang, W.G. Huang, J.Y. Jin, Y.H. Gan, S.J. Zhang, Oxygen-vacancy-mediated energy transfer for singlet oxygen generation by diketone-anchored MIL-125, *Appl. Catal. B Environ.* 292 (2021), 120197.
- [29] X. Chen, X. Duan, W. Oh, P. Zhang, C. Guan, Y. Zhu, T. Lim, Insights into nitrogen and boron-co-doped graphene toward high-performance peroxymonosulfate activation: maneuverable N-B bonding configurations and oxidation pathways, *Appl. Catal. B Environ.* 253 (2019) 419–432.
- [30] X. Lu, W. Qiu, J. Ma, H. Xu, D. Wang, H. Cheng, W. Zhang, X. He, The overestimated role of singlet oxygen for pollutants degradation in some non-photochemical systems, *Chem. Eng. J.* 401 (2020), 126128.
- [31] Y. Zhao, M. Sun, X. Wang, C. Wang, D. Lu, W. Ma, S.A. Kube, J. Ma, M. Elimelech, Janus electrocatalytic flow-through membrane enables highly selective singlet oxygen production, *Nat. Commun.* 11 (2020) 6228.
- [32] Z. Wei, H. Wang, C. Zhang, K. Xu, X. Lu, T. Lu, Reversed charge transfer and enhanced hydrogen spillover in platinum nanoclusters anchored on titanium oxide with rich oxygen vacancies boost hydrogen evolution reaction, *Angew. Chem. Int. Ed.* 60 (2021) 16622–16627.
- [33] S. Zhu, X. Li, J. Kang, X. Duan, S. Wang, Persulfate activation on crystallographic manganese oxides: mechanism of singlet oxygen evolution for nonradical selective degradation of aqueous contaminants, *Environ. Sci. Technol.* 53 (2019) 307–315.
- [34] W. Oh, Z. Dong, G. Ronn, T. Lim, Surface-active bismuth ferrite as superior peroxymonosulfate activator for aqueous sulfamethoxazole removal: performance, mechanism and quantification of sulfate radical, *J. Hazard. Mater.* 325 (2017) 71–81.
- [35] J. Jiang, X. Wang, Y. Liu, Y. Ma, T. Li, Y. Lin, T. Xie, S. Dong, Photo-Fenton degradation of emerging pollutants over Fe-POM nanoparticle/porous and ultrathin g-C₃N₄ nanosheet with rich nitrogen defect: degradation mechanism, pathways, and products toxicity assessment, *Appl. Catal. B Environ.* 278 (2020), 119349.
- [36] W.A. Arnold, Y. Oueis, M. O'Connor, J.E. Rinaman, M.G. Taggart, R.E. McCarthy, K.A. Foster, D.E. Latch, QSARs for phenols and phenolates: oxidation potential as a predictor of reaction rate constants with photochemically produced oxidants, *Environ. Sci. -Proc. Imp.* 19 (2017) 324–338.
- [37] M. Sanchez-Polo, M.M.A. Daiem, R. Ocampo-Perez, J. Rivera-Utrilla, A.J. Mota, Comparative study of the photodegradation of bisphenol A by HO[•], SO₄²⁻ and CO₃²⁻/HCO₃⁻ radicals in aqueous phase, *Sci. Total Environ.* 463 (2013) 423–431.
- [38] J. Xie, Z.P. Liao, M. Zhang, L.H. Ni, J.W. Qi, C.H. Wang, X.Y. Sun, L.J. Wang, S. B. Wang, J.S. Li, Sequential ultrafiltration-catalysis membrane for excellent removal of multiple pollutants in water, *Environ. Sci. Technol.* 55 (2021) 2652–2661.
- [39] N. Lu, H. Lin, G. Li, J. Wang, Q. Han, F. Liu, ZIF-67 derived nanofibrous catalytic membranes for ultrafast removal of antibiotics under flow-through filtration via non-radical dominated pathway, *J. Membr. Sci.* 639 (2021), 119782.
- [40] J. Zhao, F. Li, H. Wei, H. Ai, L. Gu, J. Chen, L. Zhang, M. Chi, J. Zhai, Superior performance of ZnCoO_x/peroxymonosulfate system for organic pollutants removal by enhancing singlet oxygen generation: The effect of oxygen vacancies, *Chem. Eng. J.* 409 (2021), 128150.
- [41] W. Xu, W. Xue, H. Huang, J. Wang, C. Zhong, D. Mei, Morphology controlled synthesis of α -Fe₂O₃-x with benzimidazole-modified Fe-MOFs for enhanced photo-Fenton-like catalysis, *Appl. Catal. B Environ.* 291 (2021), 120129.
- [42] A. Jawad, K. Zhan, H. Wang, A. Shahzad, Z. Zeng, J. Wang, X. Zhou, H. Ullah, Z. Chen, Z. Chen, Tuning of persulfate activation from a free radical to a nonradical pathway through the incorporation of non-redox magnesium oxide, *Environ. Sci. Technol.* 54 (2020) 2476–2488.
- [43] Y. Bai, H.Y. Wang, J.H. He, Y.T. Zhang, E.Y.X. Chen, Dual-initiating and living frustrated lewis pairs: expeditious synthesis of biobased thermoplastic elastomers, *Nat. Commun.* 12 (2021) 4874.
- [44] J. Yang, S. Hu, L. Shi, S. Hoang, W. Yang, Y. Fang, Z. Liang, C. Pan, Y. Zhu, L. Li, J. Wu, J. Hu, Y. Guo, Oxygen vacancies and lewis acid sites synergistically promoted catalytic methane combustion over perovskite oxides, *Environ. Sci. Technol.* 55 (2021) 9243–9254.
- [45] X. Wang, L. Lu, B. Wang, Z. Xu, Z. Xin, S. Yan, Z. Geng, Z. Zou, Frustrated lewis pairs accelerating CO₂ reduction on oxyhydroxide photocatalysts with surface lattice hydroxyls as a solid-state proton donor, *Adv. Funct. Mater.* 28 (2018), 1804191.
- [46] A. Khan, Z. Liao, Y. Liu, A. Jawad, J. Ifthikar, Z. Chen, Synergistic degradation of phenols using peroxymonosulfate activated by CuO-Co₃O₄@MnO₂ nanocatalyst, *J. Hazard. Mater.* 329 (2017) 262–271.
- [47] Y. Chen, G. Zhang, H. Liu, J. Qu, Confining free radicals in close vicinity to contaminants enables ultrafast Fenton-like processes in the interspacing of MoS₂, *Membr.*, *Angew. Chem. Int. Ed.* 58 (2019) 8134–8138.
- [48] Z. Wan, Z. Xu, Y. Sun, M. He, D. Hou, X. Cao, D.C.W. Tsang, Critical impact of nitrogen vacancies in nonradical carbocatalysis on nitrogen-doped graphitic biochar, *Environ. Sci. Technol.* 55 (2021) 7004–7014.
- [49] T.N. Das, Reactivity and role of SO₄²⁻ radical in aqueous medium chain oxidation of sulfite to sulfate and atmospheric sulfuric acid generation, *J. Phys. Chem. A* 105 (2001) 9142–9155.
- [50] B. Zhang, L. Zhao, J. Lin, Determination of folic acid by chemiluminescence based on peroxymonosulfate-cobalt(II) system, *Talanta* 74 (2008) 1154–1159.

[51] J.H. Lai, X.Y. Jiang, M. Zhao, S.A. Cui, J. Yang, Y.F. Li, Thickness-dependent layered $\text{Bi}_2\text{O}_3\text{O}_3$ modified with carbon quantum dots for photodegradation of bisphenol A: mechanism, pathways and DFT calculation, *Appl. Catal. B Environ.* 298 (2021), 120622.

[52] W. Liu, Y. Li, F. Liu, W. Jiang, D. Zhang, J. Liang, Visible-light-driven photocatalytic degradation of diclofenac by carbon quantum dots modified porous $\text{g-C}_3\text{N}_4$: mechanisms, degradation pathway and DFT calculation, *Water Res.* 151 (2019) 8–19.

[53] J. Wang, S. Wang, Reactive species in advanced oxidation processes: formation, identification and reaction mechanism, *Chem. Eng. J.* 401 (2020), 126158.

[54] J.L. Wang, S.Z. Wang, Effect of inorganic anions on the performance of advanced oxidation processes for degradation of organic contaminants, *Chem. Eng. J.* 411 (2021), 128392.

[55] Y. Guan, J. Ma, Y. Ren, Y. Liu, J. Xiao, L. Lin, C. Zhang, Efficient degradation of atrazine by magnetic porous copper ferrite catalyzed peroxymonosulfate oxidation via the formation of hydroxyl and sulfate radicals, *Water Res.* 47 (2013) 5431–5438.